DOI: 10.1002/ ((please add manuscript number))
Article type: Full Paper

Multifunctional Recyclable Electronic Skins Enabled by Hierarchical Dynamic Network Structures

Xiaohui Yu, Choon Peng Teng, Jayven Chee Chuan Yeo, Xiaotong Fan*, Xiaoshan Fan, Tianxi Liu*, Zibiao Li*

Xiaohui Yu
College of Material and Textile Engineering, Jiaxing University, Jiaxing 314001, People's Republic of China.

Xiaohui Yu, Xiaoshan Fan, and Tianxi Liu
State Key Laboratory for Modification of Chemical Fibers and Polymer Materials, College of Materials Science and Engineering, Donghua University, Shanghai 201620, People's Republic of China.

Xiaohui Yu, Xiaotong Fan, and Zibiao Li
Institute of Sustainability for Chemicals, Energy and Environment (ISCE2), Agency for Science, Technology and Research (A*STAR), 1 Pesek Road, Jurong Island, Singapore 627833, Republic of Singapore
E-mail: xiaotong_fan@isce2.a-star.edu.sg

Zibiao Li, Choon Peng Teng, Jayven Chee Chuan Yeo
Institute of Materials Research and Engineering (IMRE), Agency for Science, Technology and Research (A*STAR), Singapore 138634, Republic of Singapore
E-mail: lizb@imre.a-star.edu.sg

Zibiao Li
Department of Materials Science and Engineering, National University ofSingapore, 9 Engineering Drive 1, Singapore 117576, Republic of Singapore

Tianxi Liu
Key Laboratory of Synthetic and Biological Colloids, Ministry of Education, School of Chemical and Material Engineering, International Joint Research Laboratory for Nano Energy Composites, Jiangnan University, Wuxi, Jiangsu 214122, People's Republic of China
E-mail: txliu@jiangnan.edu.cn

Keywords: Recyclable, ionogels, electronic skins, dynamic network structures

Abstract: Inspired by the sensory functions of the human skin, the development of electronic skins (e-skins) has garnered significant attention. Ionogels, as emerging class of soft materials, shows promise in serving as e-skins. The pursuit of a sustainable society motivates the development of recyclable ionogels, typically achieved by introducing dynamic non-covalent bonds. However, these current state-of-the-art methods often result in poor elasticity or strain softening, which significantly limits their suitability for e-skin applications. This study introduces a multifunctional and recyclable e-skin based on a hierarchical dynamic double-network ionogel that integrates dynamic covalent bonds and non-covalent interactions. This ionogel

seamlessly integrates key functions of human skin, including strain-stiffening capability, self-healing ability within 12 h, rapid response time (120 ms), and high elasticity (energy loss coefficient of 0.07 at 150% strain), all within a single material. The dynamic covalent bonds enhance cohesive energy, ensuring high elasticity, while the non-covalent bonds improve adhesive properties. As a proof of concept, the ionogel could be fabricated into a strain-temperature dual-modal e-skin, exhibiting high sensitivity, reliability, and state-independent performance. This advancement highlights the potential of ionogels in the development of next-generation recyclable wearable electronic devices.

1. Introduction

Skin, the largest organ covering the human body, shows a multitude of functions and plays a vital role in protecting the inner soft tissues and responding to various external stimuli in mediating our interactions with the world (**Figure 1A**).[1] Unlike many synthetic materials, human skin exhibits a unique nonlinear stress–strain mechanoresponsive behavior.[2] It is initially soft to the touch but rapidly stiffens to prevent external injury, thanks to a sharp increase in elastic modulus at large strains. This distinctive strain-stiffening behavior embodies a fundamental self-defense mechanism in nature. Meanwhile, human skin is self-healable and can autonomously heal after external damage to restore its mechanical properties.[3] In addition, the skin also has sensitive sensory functions, which could respond to various external stimuli (e.g., pressure, temperature, humidity, and other physiological parameters).[4] Inspired by the ion-conducting nature and sensory functions of the skin, various materials such as metals, carbon nanotubes, and conductive polymers have been developed for strain and temperature sensing.[5] However, the inherent stretchability of skin has driven researchers to explore soft materials like gels for electronic skin fabrication. In recent years, a new class of gels known as ionogels has emerged, consisting of cross-linked polymer networks and ionic liquids (ILs).[6] Due to the inherent high conductivity, low volatility, extensive thermal stability, and cost-effectiveness of ILs, ionogels are poised to replace hydrogels as flexible electronics for e-skins.[7] This substitution holds immense promise in energy, electronics, and environmental science. However, it remains a significant challenge to design the ionogels engaging such multiple functions of self-healability, strain-stiffening capability, and sensitive multimodal sensing performance.

The pursuit of a sustainable society motivates the development of recyclable ionogels, typically achieved by introducing dynamic non-covalent bonds, such as hydrogen bonding, metal coordination, or van der Waals forces into the ionogels.[6b, 8] However, non-covalent bonds often result in poor elasticity or strain softening of the ionogels.[9] As non-covalent bonds break and reform under strain, they enable polymer chains to relax and dissipate energy, leading to high hysteresis and diminished mechanical performance during cyclic deformation. The strain-stiffening capability of the skin-like materials lies in designing hierarchical cross-linked networks, which concurrently possess stable covalent bonds and weak non-covalent interactions.[10] However, this approach presents a conflict between the covalently cross-linked

networks and the desired recyclability. A promising strategy to resolve this challenge is the incorporation of dynamic covalent bonds into ionogels, alongside dynamic non-covalent bonds, to produce recyclable, strain-stiffening ionogels.[2a] Dynamic covalent bonds are stable under operating conditions, but can be disrupted and rearranged when exposed to external stimuli, such as reducing/oxidizing agents, temperature changes, or light.[11] This enables ionogels to maintain robust cross-links while being recyclable and stimuli-responsive self-healing in response to mild stimulation, thereby extending the lifespan of ionogel-based e-skin.

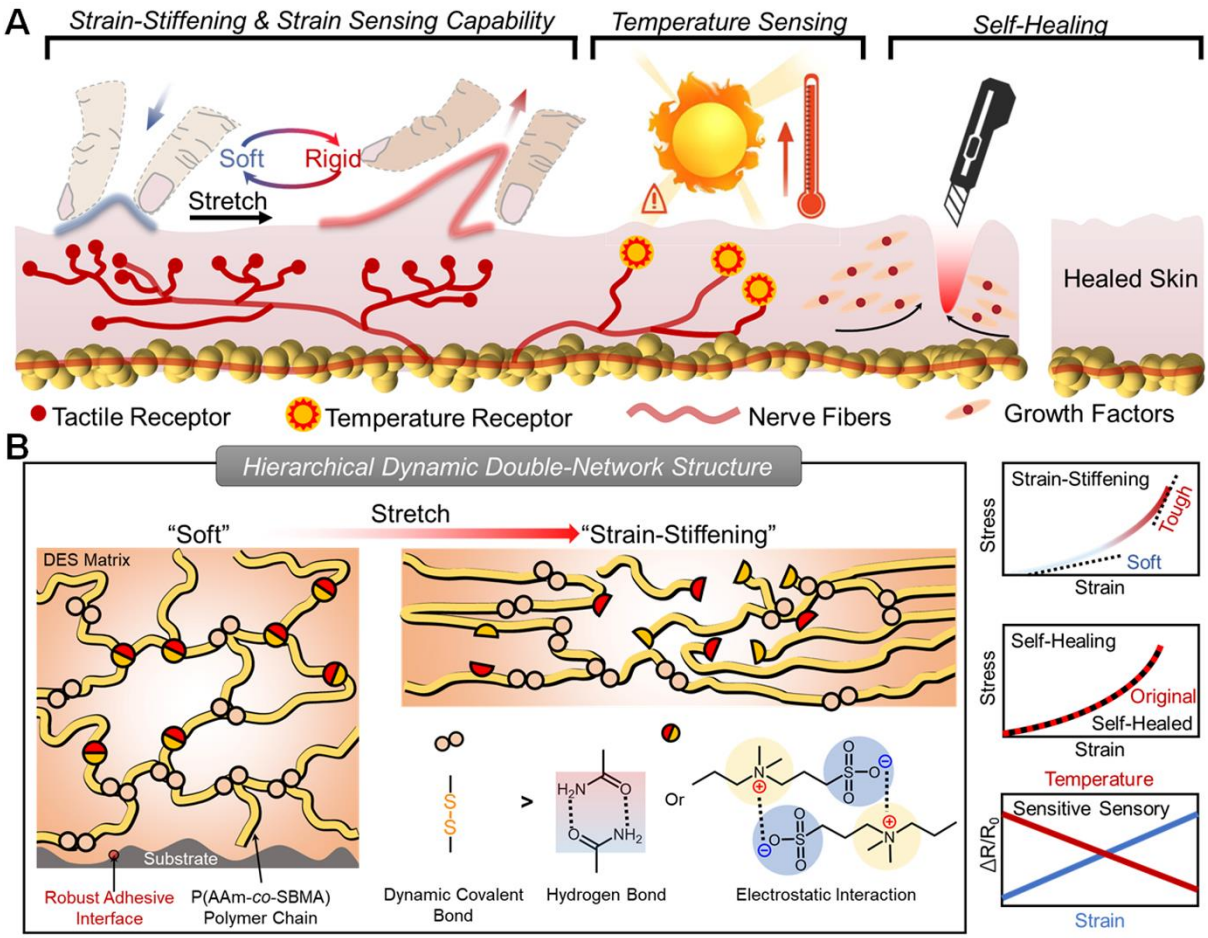

Figure 1. The design of the hierarchical dynamic double-network ionogel-based strain-temperature dual modal e-skin. A) The multi-functionality of human skin, including strain-stiffening, strain sensing, temperature sensing, and self-healing capability; **B)** Design of the functional ionogel featured with hierarchical dynamic double-network structure.

Meanwhile, we know that if an e-skin is to achieve high-precision detection, it needs to have high adhesiveness and excellent elasticity.[12] Ensuring reliable self-adhesiveness is crucial to prevent interfacial defects or delamination, guaranteeing the

sensor's usage stability and high sensitivity.[13] Deep eutectic solvents (DESs) have been recently used to develop strong adhesives with enhanced interfacial bonding due to multiple supramolecular interactions, which dynamically interact with polymer chains.[14] However, conventional adhesive DESs-based ionogels often exhibit low cohesive energy, resulting in significant hysteresis during tensile cycling.[15] This poor elasticity is detrimental to ideal epidermal electronics and leads to undesirable state-dependent characteristics. Specifically, poor elasticity can cause different relative resistance change (R/R_0) values in the sensing process, due to the material state changes during stretching, which will significantly influence the sensing performance.[16] Therefore, integrating self-adhesion and high elasticity into a single artificial material is crucial for fabricating functional and sensitive e-skin.[17] To the best of our knowledge, there have been no reports on ionogels with the combined attributes of good elasticity, high adhesiveness, full self-healability, and unique strain-stiffening properties.

In this study, we report a multifunctional, recyclable e-skin based on a hierarchical dynamic double-network ionogel, uniquely integrateing strain-stiffening, complete self-healing ability, high adhesiveness, and exceptional elasticity (**Figure 1B**). This innovative design leverages a robust yet dynamic covalent disulfide bond-based primary network and a secondary network of non-covalent interactions, enabling the seamless integration of recyclability, high adhesiveness (45.5 kPa on steel, 49.2 kPa on glass, and 25.3 kPa on pig skin), self-healing within 12 h (tensile length self-healing efficiency of 94.5%), high elasticity (energy loss coefficient of 0.07 at 150% strain), rapid response time (120 ms), and strain-stiffening behavior—something that has not been achieved in previous ionogel systems. The remarkable adhesion to diverse substrates originates from the abundant hydrogen bonding and electrostatic interactions, while dynamic covalent cross-links enhance the cohesive energy, minimizing entanglements and ensuring high elasticity. Notably, this ionogel uniquely combines high elasticity with efficient self-healing capability, addressing the long-standing challenge in self-healing materials. As a proof of concept, we demonstrate the ionogel’s application as a strain-temperature dual-modal e-skin for real-time , reliable human motion monitoring. Our findings advance the design of multifunctional ionogels and pave the way for next-generation high-performance, recyclable e-skin devices.

2. Results and Discussion

2.1. Design, Preparation and Characterization of the Ionogels

The multifunctional hierarchical dynamic double-network ionogel (HDDNI) containing poly(acrylamide-*co*-[(2-(methacryloyloxy) ethyl] dimethyl-(3-sulfopropyl) ammonium hydroxide) (P(AAm-*co*-SBMA)) was prepared through convenient one-pot free radical copolymerization of their corresponding monomers in DES. Concurrently, dynamic covalently cross-linking was achieved by the disulfide bond-based cross-linker N,N'-bis(acryloyl)cystamine (BAC) during the copolymerization process, forming a three-dimensional cross-linked network **(Scheme S1**).[18] Zwitterionic SBMA monomer was included in the system to improve the durability of the prepared ionogel by facilitating the formation of a hydration shell without compromising hydrogen bonds.[19] DES was prepared by mixing choline chloride (ChCl) and glycerol at 90 °C for 30 minutes without additional purification steps. Among them, ChCl served as a hydrogen bond acceptor (HBA), while glycerol acted as a hydrogen bond donor (HBD). Due to the strong interaction between HBA and HBD, this ChCl-glycerol DES exhibits a low freezing point and volatility. Furthermore, the electrostatic interactions of the N^+-Cl^- bonds enhanced the ionic properties of the DES, potentially contributing to the good conductivity of the DES-based ionogel. Hence, the ChCl-glycerol DES was chosen as a substitute for traditional conductive hydrogel solvents. The hierarchical dynamic double-network ionogels were denoted as HDDNI-χ (χ = 1, 2, 3), where the concentration of BAC was 0.3, 0.6, and 0.9%, respectively. For comparison, the hierarchical non-dynamic double-network ionogel (HNDNI) was synthesized using N,N'-methylenebisacrylamide (MBAA) as the cross-linker, with conditions identical to those for HDDNI-2 (**Scheme S1**). The dynamic single-network ionogel (DSNI) was also prepared without any cross-linker, under the same conditions as HDDNI-2. Additionally, the P(AAm-co-SBMA) hydrogel was synthesized using water as the solvent instead of DES, without any cross-linker, while maintaining the other conditions as in HDDNI-2.

The incorporation of DES imparted HDDNI good environmental stability. Initially, HDDNI retained a gel-like state at extremely low temperatures (-20 °C), as indicated by the absence of any significant peaks in the differential scanning calorimetry (DSC) curve (**Figure S1A**). On the contrary, when water was the solvent, the P(AAm-*co*-SBMA) based hydrogel was frozen into the glass state and lost its treatment flexibility under this low temperature. The sharp peak located at 1.9 °C, corresponding to the freezing point, further confirms its poor resistance to freezing (**Figure S1B**). The long-

term stability of HDDNI was demonstrated by its consistent performance, which was measured at various storage times at different storage temperatures. Due to the evaporation of water in the hydrogels, the weight of the P(AAm-*co*-SBMA) based hydrogel decreased to only ≈20% of its original state after 3 days under normal conditions, eventually transforming into a dried polymer state (**Figure S2**). The evaporation rate was found to increase with temperature. As the storage temperature rose to 60 °C, the weight of the P(AAm-*co*-SBMA) based hydrogel decreased rapidly, approaching the water content after the initial 2 days. Conversely, the weight of the HDDNI was maintained stable in different conditions during the long storage time. Simultaneously, the conductivity of HDDNI remained stable without significant changes, demonstrating clear superiority over the P(AAm-*co*-SBMA) based hydrogel (**Figure S3**). These results confirmed that the electrical percolation paths within the HDDNI were relatively stable, and the fabricated ionogels were suitable for use across a wide range of temperatures in open air.

Figure 2A illustrates the network structure of the fabricated ionogels. As we all know, the multiple supramolecular interactions, including the hydrogen bonding and electrostatic interactions, imparted the DSNI with a single dynamic supramolecular cross-linked network. Thanks to the introduction of covalent cross-linkers, the second network was successfully constructed to form the hierarchical cross-linked network in HDDNI, and HNDNI. The chemical structure of the samples composited of P(AAm-*co*-SBMA) polymer chains and DES matrix was investigated by FT-IR (**Figure S4**).[20] The P(AAm-co-SBMA) segments exhibited characteristic peaks at 2930, 1666, and 1620 cm^{-1}, corresponding to -CH_2 stretching, C=O bending, and N-H in-plane bending in the NH_2C=O group of PAAm segments, respectively. Additionally, absorption peaks at 1733 and 1454 cm^{-1} are attributed to ester groups and C-H stretching of -N^+-$(CH_3)_2$- groups on PSBMA segments. The peaks at 1037 and 1188 cm^{-1} mainly arise from the symmetric and asymmetric stretching vibrations of -SO_3- groups.

All samples displayed a gel-like state due to the construction of the cross-linking networks, as evidenced by the storage modulus (G') being higher than the loss modulus (G") in the plateau region (**Figure S5**). Notably, the plateau modulus (Gp) of HDDNI and HNDNI surpassed that of DSNI, indicating the formation of the second covalently cross-linked network. As the shearing amplitude increased, a distinct transition point could be observed, indicating the rupture of the cross-linked polymer networks. Moreover, all samples exhibited excellent frequency stability over a wide

frequency range (**Figure S6**). The cross-linking strength of the ionogels was investigated by the relaxation experiments, as illustrated in **Figure S7**. The samples underwent rapid deformation to an amplitude of 10% and were subsequently allowed to relax for 1,000 seconds. HDDNI and HNDNI exhibited creep resistance compared to DSNI, which is attributed to their covalently cross-linked networks. The ratio of residual modulus to initial modulus of HDDNI (5.6%) and HNDNI (4.1%) were both significantly higher than the values of DSNI (1.1%). A higher ratio indicated stronger cross-linking within the polymeric network and vice versa. The equilibrium swelling ratio (ESR = w/w_0) of water was also determined to quantify the cross-linking densities, following methods from previous studies.[17b] Herein, w_0 and w represented the weight of the initial and fully swollen ionogel. The formation of the covalently cross-linked network enabled low ESR values for both HDDNI and HNDNI, at 8.32 and 9.17, respectively.

Furthermore, the effective cross-linking density, (υ_e), is a fundamental parameter that reflects the network structure of polymeric materials. This parameter is crucial for understanding the structure–property relationships of polymer networks, as it directly impacts their mechanical properties, elasticity, swelling behavior, and energy dissipation mechanisms. In this work, the effective cross-linking density was calculated following the reported work (see detailed in Supporting Information).[21] The calculated values for HNDNI and HDDNI were 50.98 mol/m³ and 49.75 mol/m³, respectively. Despite the structural differences between the cross-linkers—BAC for HDDNI, featuring dynamic disulfide bonds, and MBAA for HNDNI, forming stable covalent bonds—the overall cross-linking density remained comparable under identical synthesis conditions. This similarity resulted in the analogous mechanical properties observed for the two materials.

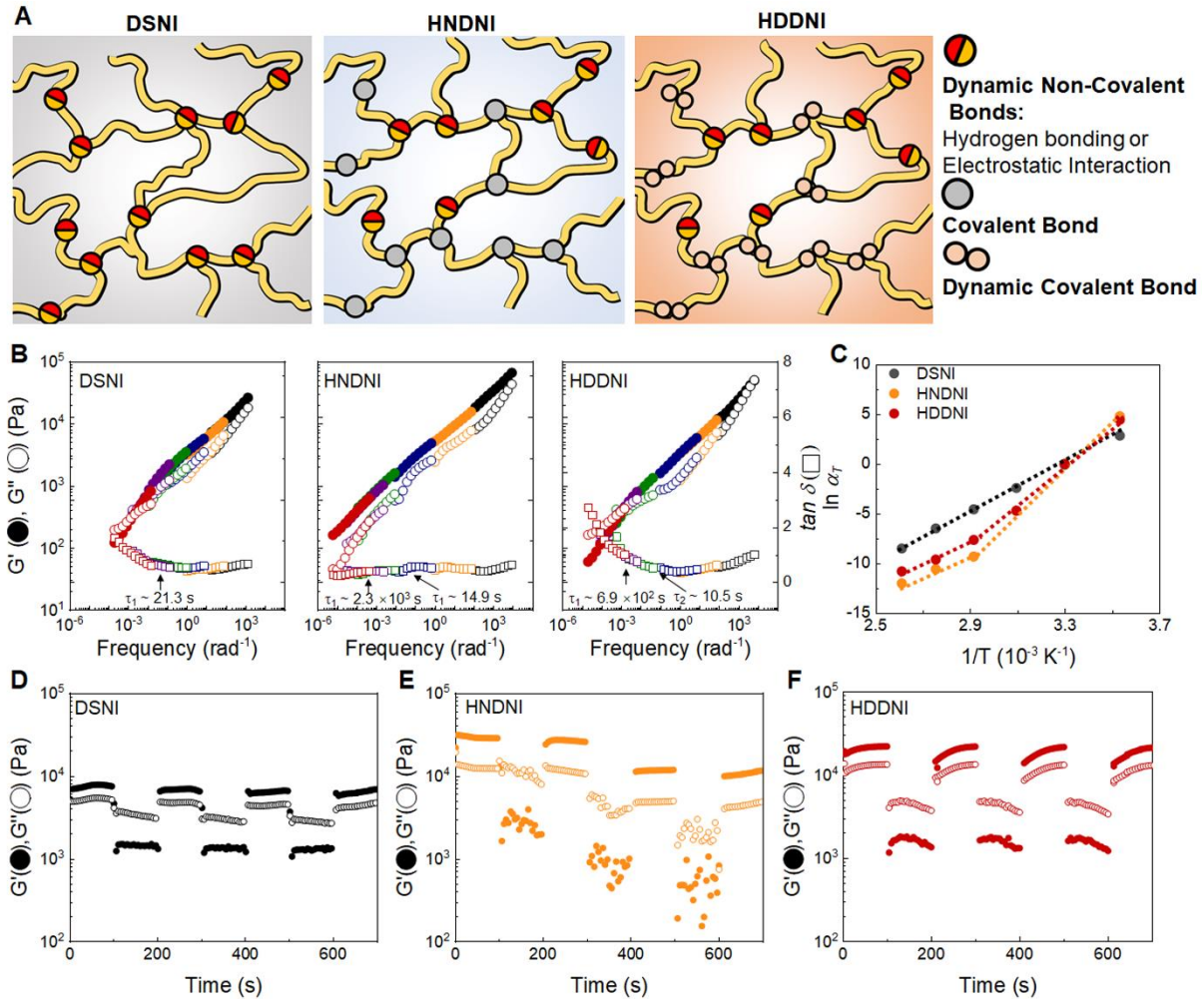

Figure 2. Hierarchical dynamic double-network structure of the ionogels. A) Schematic illustration of the dynamic single-network, hierarchical covalent double-network, and hierarchical dynamic double-network structure of the designed ionogels; **B)** The frequency dependence of the storage modulus (G'), loss modulus (G''), and loss factor (tanδ) of DSNI, HNDNI, and HDDNI; **C)** The Arrhenius plot of the above corresponding samples; The dynamic alternating strain–time sweeping curves of **D)** DSNI, **E)** HNDNI, and **F)** HDDNI at room temperature.

Dynamic rheological measurements were performed to characterize the intrinsic hierarchical network, applying the time-temperature superposition (TTS) principle with a reference temperature of 30 °C (constructed by six frequency sweeping curves conducted at 10, 30, 50, 70, 90, and 110 °C).[22] As depicted in **Figure 2B**, a notable frequency dependence was observed across a broad frequency range for all samples. In the case of DSNI, the tanδ master curve increased as the frequency decreased, exhibiting a single peak around ~4.7 × 10^{-2} rad s^{-1}, corresponding to a relaxation time (τ) of approximately 1/(~4.7 × 10^{-2}) ≈ 21.3 s. This result suggests that the supramolecular interaction-based cross-linking network has a relaxation time of 21.3

s, indicating a weak network. The apparent activation energy (E_a) for DSNI was estimated to be 59.2 kJ mol^{-1} using the Arrhenius equation with the frequency-scale shift factor (α_T) from the corresponding Arrhenius plot (**Figure 2C**). In comparison, the master curve of HDDNI exhibited two peaks at frequencies of 6.7×10^{-2} ($\tau \sim 14.9$ s) and 4.3×10^{-4} rad s^{-1} ($\tau \sim 2.3 \times 10^{3}$ s). The two different E_a values of 62.7 and 104.5 kJ mol^{-1} for HDDNI were obtained from the Arrhenius plots, indicating the successful construction of the hierarchical network. Among these, the disulfide bond and supramolecular interactions served as the strong and weak bonds, respectively. In contrast, HNDNI showed no sol-gel transition occurring in the low-frequency range due to the lack of dynamic covalent bonds.

Meanwhile, the ionogels also demonstrated intriguing dynamic characteristics attributed to their well-designed network structure. As shown in **Figure 2D-F**, all the samples showed remarkable stability under a small shearing strain of 5% for 100 s, indicating their stable mechanical properties. However, upon increasing the amplitude oscillation to 100%, a critical transition occurred where the G'' exceeded the G', leading to a sol-like state. This transition highlighted the unique rheological behavior of the ionogels, underlining their dynamic response to varying mechanical stimuli. Upon reverting the shearing strain back to 1%, a notable recovery phenomenon was observed as the ionogels seamlessly returned to their initial gel-like state. This self-recovery ability is a pivotal trait for materials intended for prolonged usage, demonstrating the ionogels' potential for sustainable applications. When comparing different samples, DSNI and HDDNI showcased a high recovery efficiency of the modulus, approximately 90%. This efficient recovery capability could be attributed to the dynamic nature of their cross-linked network, allowing for reversible bond formation and breakage in response to external stimulis. In contrast, HNDNI exhibited poor self-recoverability with low efficiency, primarily due to the non-dynamic characteristic of its covalent cross-linked linkage. This difference in recovery efficiency underscored the crucial role of the dynamic cross-linked network in determining the self-healing properties of the ionogels.

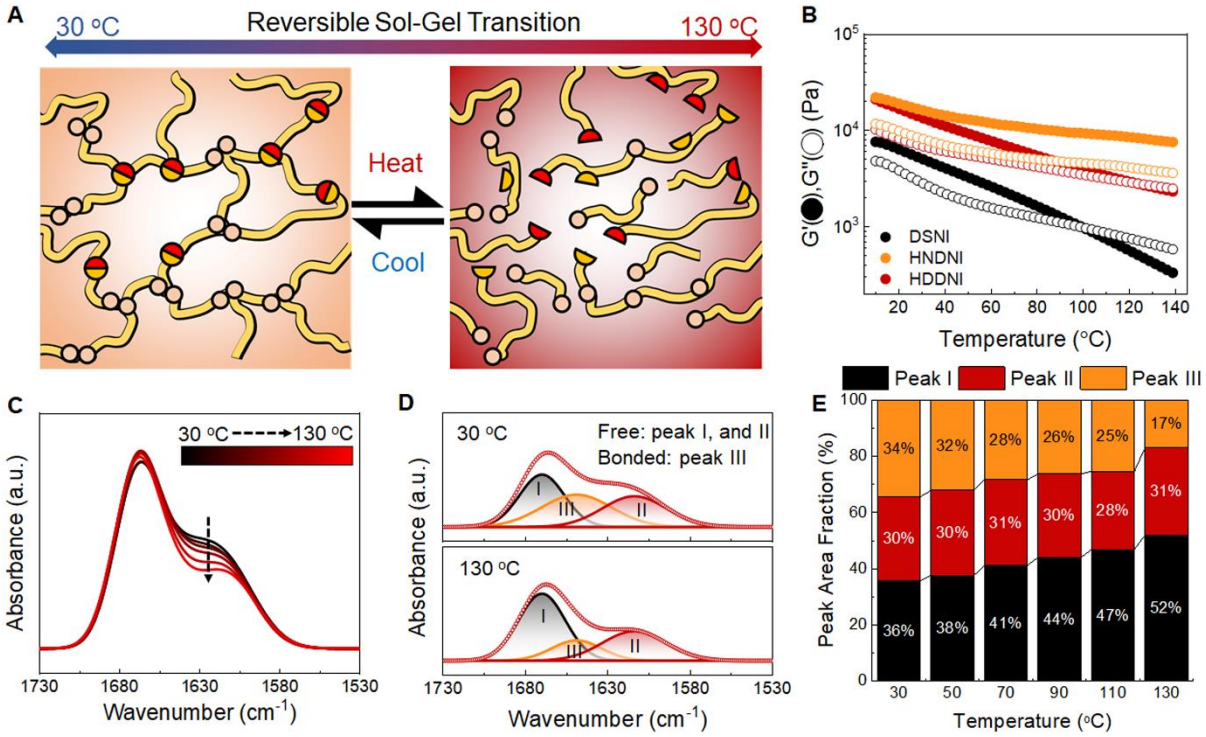

Figure 3. The sol-gel transition behavior of ionogels and the elucidation of its underlying mechanism. A) Schematic illustration of the sol-gel transition process of HDDNI; **B)** Temperature sweeping curves of DSNI, HNDNI, and HDDNI; **C)** Variable-temperature FT-IR spectra of HDDNI peaks corresponding to carbonyl bands (C=O) associated with hydrogen bonds; **D)** FT-IR spectra of HDDNI in the C=O stretching vibration region at 30 and 130 °C, respectively; **E)** Summary of the assignment of the deconvoluted subpeaks of the C=O absorption bands at different temperatures.

Notably, the G' and G" of HDDNI and DSNI displayed intriguing sol-gel transition behavior, endowing these ionogels with potential thermoplastic characteristics (as illustrated in **Figure 3A**). As the temperature rose to 140 °C, the G' of DSNI dropped to ~10^2 level, and an obvious sol-gel transition point was observed at 98.1 °C (**Figure 3B**). The G' of HDDNI exhibited a slight decline below 100 °C due to the dissociation of supramolecular interactions. Meanwhile, the exchange of the disulfide bonds also imparted the ionogel with intriguing thermal dynamic characteristics, with a sol-gel transition occurring at 126.3 °C. In contrast, the modulus curves of HNDNI showed no sol-gel transition point due to the lack of dynamic covalent bonds. Furthermore, the temperature-dependent FT-IR analysis was conducted on the samples to reveal the above sol-gel transition behavior of their dynamic cross-linked network.[23] The intensity of the infrared absorption peaks corresponding to carbonyl bands (C=O) associated with hydrogen bonds increased from 30 to 130 °C (**Figure 3C**). Specifically, the deconvoluted subpeaks could be assigned to the free C=O (peak I: 1670 cm^{-1}), free NH_2C=O (peak II: 1610 cm^{-1}), and the hydrogen-bonded C=O (peak III: 1649 cm^{-1})

within the carboxyl group. Quantitative analysis revealed that the fraction of hydrogen-bonded C=O in HDDNI at 30 °C (34%) was significantly higher than that at 130 °C (17%) (as shown in **Figure 3D** and **Figure S8**, and summarized in **Figure 3E**), indicating the dissociation and weakening of hydrogen bonds with increasing temperature. Additionally, the C-H stretching of $-N^{+}-(CH_3)_2-$ groups on PSBMA segments decreased and blue-shifted, while the peak corresponding to $-SO_3-$ groups increased and red-shifted, indicating the weakening of electrostatic interactions (**Figure S9**). Additionally, disulfide groups could undergo cleavage through a reduction reaction, forming two thiol groups, which could then be re-formed through an oxidation reaction.[24] These fast thiol-disulfide exchange reactions render these linkages reversible under mild conditions, providing the second covalent disulfide bonds cross-linked network with intriguing dynamic characteristics.

2.2. Skin-Like Mechanical Performance and Recyclability of the Ionogels

The hierarchical dynamic double-network created in this system endowed the ionogels with skin-like mechanical properties, including high stretchability, low hysteresis, efficient self-healing capability, and intriguing strain-stiffening performance. As shown in the tensile curves, all the samples showed good stretchability of over 1000%, which far exceeded human skin deformation during various activities. As shown in **Figure 4A**, DSNI, which was cross-linked only through non-covalent interactions, showed evident mechanical yield and lacks sufficient strength due to the absence of covalent bonds. This lower strength was likely due to the dynamic and relatively fast movement of polymer chains within its non-covalently cross-linked network. In contrast, while HNDNI had a covalently cross-linked network that provides enhanced mechanical strength, it lacks dynamic covalent bonds, which were critical for self-healing capabilities. This limitation prevented HNDNI from recovering its mechanical properties after external damage, making it less suitable for applications requiring both durability and self-healing. To address these limitations, we designed and introduced a hierarchical dynamic double-network in HDDNI. This structure combined a robust yet dynamic covalent disulfide bond-based primary network with a secondary network formed by multiple weak non-covalent interactions. The resulting hierarchical network structure endowed HDDNI with both significantly enhanced mechanical strength and remarkable self-healing ability.

To further optimize HDDNI's performance, we adjusted the concentration of the BAC cross-linker within the system. The tensile properties of HDDNI depend strongly on the cross-linker content, which directly affected the cross-linking density, and thus the flexibility and strength of the ionogel. As summarized in **Figure 4B**, HDDNI-2 achieves the highest tensile strength (390 kPa), elongation at break (1845%), and overall toughness (355 kJ m^{-3}) among all samples. This optimized cross-linking density strikes an ideal balance between rigidity and flexibility. By contrast, HDDNI-1, with a lower cross-linker content, exhibited only half the tensile strength of HDDNI-2 due to a looser network that lack the cohesion needed to support high loads. Meanwhile, HDDNI-3, with a higher cross-linker concentration, had increased internal cross-linking density, which, while enhancing rigidity, restricts polymer chain mobility. This constraint reduced its elongation at break to approximately 1250%, indicating a trade-off between network flexibility and stretchability. In conclusion, HDDNI-2 demonstrated the best balance of strength, toughness, and flexibility, establishing it as the optimal candidate for further research and application.

To provide a more intuitive observation of the ionogel's self-healing capability, we conducted an experiment where the HDDNI was cut in half. The two halves were then brought into contact and left at 80 ℃ for 12 hours without any external stimulation. After self-healing, the healed ionogel sample was still stretchable (**Figure S10, Video S1 and S2**). The mechanical properties of the self-healed DSNI and HDDNIs exhibited nearly complete recovery to their initial state after healing (**Figure 4A**). Notably, HDDNI exhibited self-healing capability comparable to DSNI (as summarized in **Figure 4B**). However, HNDNI showed poor self-healing capability. To quantitatively characterize the self-healing efficiency of the samples, the tensile length self-healing efficiency (η_l) and tensile strength self-healing efficiency (η_p) were calculated using the method reported in the literature.[25] Among them, DSNI showed highest self-healing efficiency with η_l and η_p of 97.5% and 92.4%, respectively. With the introduction of dynamic covalent cross-linkers, the self-healing efficiency of HDDNI was slightly lower than that of DSNI. Specifically, HDDNI-2 exhibits self-healing efficiencies (η_l and η_p) of 94.5% and 89.7%, respectively. As summarized in **Figure S11**, the self-healing efficiency of HDDNIs decreases with increasing cross-linker content. This could be attributed to the increase in cross-linking density, which restricted the free movement of polymer chains,

thereby limiting the self-healing efficiency. These results were consistent with the findings from the rheological measurements mentioned earlier.

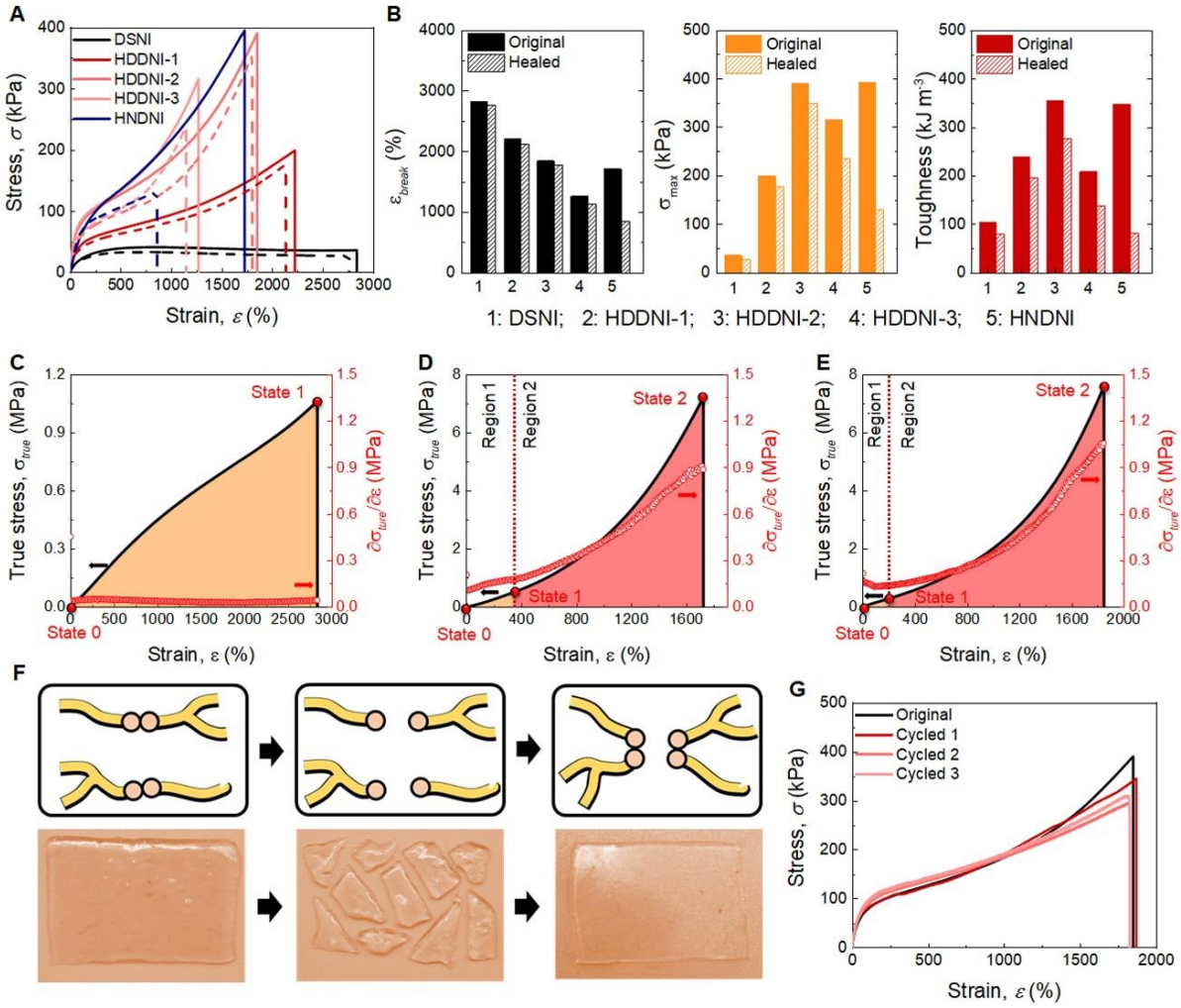

Figure 4. Mechanical robustness and recyclability of the ionogels. A) Tensile curves of the HDDNI, HNDNI, and DSNI (dotted lines are the tensile curves of self-healed samples); **B)** Summary of the ε_{break}, σ_{max}, and toughness of the prepared ionogels; Typical true stress curves and their first derivative line of **C)** DSNI, **D)** HNDNI, and **E)** HDDNI; **F)** Digital photographs showing the reprocessing cycle of HDDNI as a typical example; **G)** Tensile curves of the original and recycled HDDNIs.

Remarkably, HDDNI exhibited a distinct strain-stiffening mechanoresponsive behavior similar to human skin. To further evaluate its nonlinear mechanical characteristics, we analyzed the true stress curves and their corresponding first derivative curves (∂true stress/∂strain).[26] At first, the first derivative curve of DSNI was linear without strain-stiffening performance (**Figure 4C**). In contrast, due to the similar hierarchical network, HNDNI also showed strain-stiffening capability (**Figure 4D**). **Figure 4E** illustrates the mechanical behavior of HDDNI, which can be divided into two

regions with three states based on different deformation ranges. In state 0, HDDNI exhibited a high initial modulus. Within Region 1 (0~200%), the supramolecular interaction cross-linking network in the polymer matrix breaks, decreasing the ionogel's modulus. In Region 2, further stretching into a large strain until reaching the elongation at break, the modulus of HDDNI increased to approximately 1.05 MPa, nearly eight times the original modulus (0.13 MPa). The increase in modulus could be attributed to the existence of the robust covalently cross-linking point. The unique mechanoresponsive behavior seen in HDDNI and HNDNI was reminiscent of that observed in human skin.

The recyclable regeneration ability of the traditional ionogels has been challenging to achieve due to the non-dynamic characteristic of the covalent cross-linking point. Thanks to the reversible dynamic disulfide bonds, along with non-covalent interactions such as hydrogen bonds and ionic bonds, HDDNI could be recycled and reused.[27] After being cut into small pieces, HDDNI underwent reprocessing through hot pressing at 140 °C for 1 hour to facilitate the rearrangement of polymer networks (**Figure 4F**). We conducted multiple cycles of cutting and remolding the sample, evaluating its recyclability by examining its structure and mechanical properties after each cycle. The tensile curves of remolded samples closely mirrored those of the original sample, confirming the complete recovery of its mechanical properties after reprocessing **(Figure 4G)**.

Tensile cyclic stretching/releasing tests were executed to investigate the energy dissipation mechanism of the ionogels. In **Figures 5A-C**, an obvious hysteresis loop could be observed for DSNI during the loading-unloading test, with a maximum strain of 200%, indicating substantial dissipated work. This behavior could be ascribed to the disruption of the non-covalently cross-linked network. Conversely, both HDDNI and HNDNI exhibited superior and comparable elasticity.

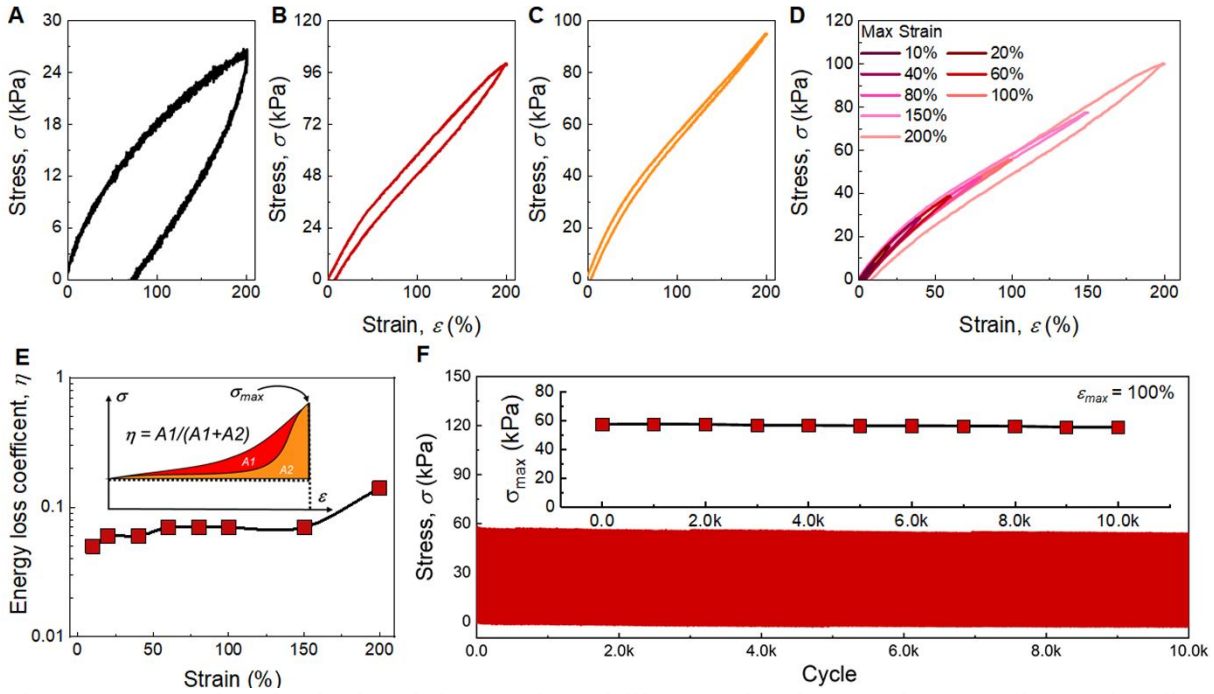

Figure 5. Mechanical elasticity and stability of the ionogels. Loading-unloading tensile curve of **A)** DSNI, **B)** HDDNI, and **C)** HNDNI; **D)** Cyclic loading–unloading stress–strain curves of HDDNI at the maximum strain of 10, 20, 40, 60, 80, 100, 150, and 200%; **E)** Summary of the energy loss coefficient (η) in different maximum strains; **F)** Consecutive 10000 cycles cyclic tensile curves of HDDNI (inset: the summary of maximum stress during the cyclic test).

To delve deeper into the dynamic mechanical properties of HDDNI, various cyclic loading-unloading tests were performed at different strains. At low strain levels (<150%), comparable to the maximum strain of human skin, the loading–unloading curves showed significant superimpose with minimal hysteresis loops (**Figure 5D**). The resultant good elasticity could be attributed to the constructed covalently disulfide bond-based cross-linked network, which mitigated most temporary entanglements and reduced energy dissipation. The energy loss coefficient (***η***), representing the efficiency of energy dissipation, was only ~0.07 in this range (**Figure 5E**).[17] Upon surpassing a strain of 200%, hysteresis loops became apparent, suggesting the dissipation of some work done. Furthermore, a series of 10000 continuous stretching cyclic tests were conducted at a strain of 100%. As shown in **Figure 5F**, the baseline and maximum stress of the tensile curves remained stable throughout the testing, indicating robust mechanical stability of HDDNI-2. As clearly illustrated in the enlarged curves, HDDNI exhibited remarkably stable mechanical performance, evidenced by the consistent and unwavering maximum stress values throughout the process (**Figure S12A**). Additionally, as shown in **Figure S12B**, we observed that aside from an initial higher energy dissipation in the first loading -unloading cycle, likely due to the

disentanglement of polymer chains within the ionogel network, the subsequent stress-strain curves demonstrate low hysteresis and overlap closely. This result suggested that HDDNI-2 maintains a stable mechanical performance during repeated cycling. To further assess the damping capacity of HDDNI-2, we calculated the energy loss coefficient over the 10,000 cycles at 100% strain. As summarized in **Figure S12C**, η of the sample remains ~0.07, signifying consistent elasticity and excellent damping stability across the cycles. These above results demonstrated the exceptional elasticity and fatigue resistance of HDDNI, which hold significant promise for applications in flexible sensors.

2.3. Bio-interface Adhesion and Compatibility of the Ionogels

To our best knowledge, the adhesion property was also crucial for flexible wearable devices, ensuring a stable connection to the substrate for accurate signal recording. In this work, HDDNI exhibited strong adhesion to various substrates such as steel, glass, and skin, showcasing its excellent interfacial adhesiveness (**Video S3**). This exceptional adhesive property of HDDNI could be attributed to the synergistic effects of hydrogen bonds, metal complexation, electrostatic interactions, ion–dipole interactions, and van der Waals forces between HDDNI matrix and substrates (as illustrated in **Figure 6A**).

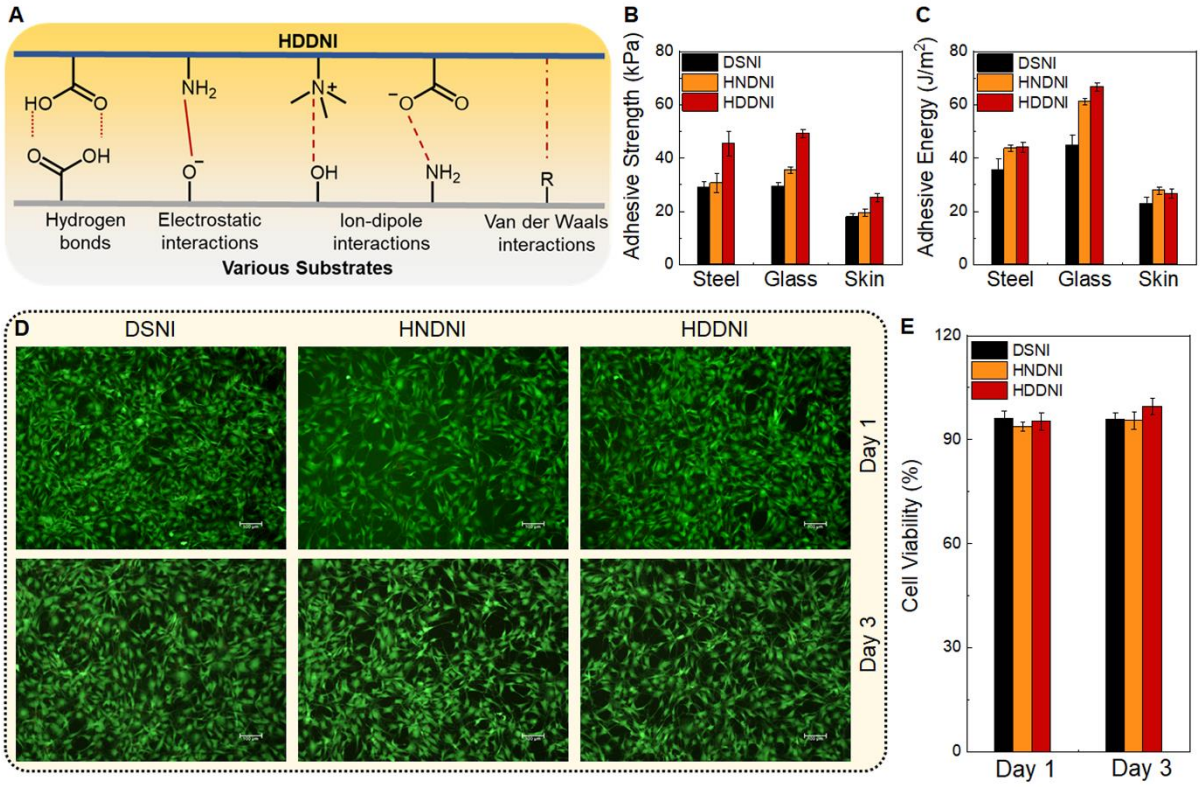

Figure 6. Bio-interface adhesion and compatibility of the ionogels. A) Schematic illustration of the interactions between the ionogel and the adherend substrates; Summary of the **B)** adhesive strength and **C)** adhesive energy of different samples on various substrates; **D)** Live (green) and dead (red) images of NIH/3T3 mouse fibroblast cells in DSNI, HNDNI, and HDDNI samples after 1 day and 3 days; **E)** Cytotoxicity experiment of different samples after 1 day and 3 days of cultivation, respectively.

To quantitatively evaluate the adhesion properties, a lap shear adhesive test was conducted following the method in reported papers.[28] The peeling force curves revealed that the shearing displacements exceeded the ionogel's length (15 mm), indicating the samples were stuck to and stretched by up and down adherends (**Figure S13**). As summarized in **Figure 6B**, the adhesion strength of HDDNI was measured at 45.5 kPa on steel, 49.2 kPa on glass, and 25.3 kPa on pig skin. The adhesive energy of HDDNI was also determined for these substrates, with values of 44.1, 66.7, and 26.7 J m^{-2} when adhered to steel, glass, and pig skin, respectively (**Figure 6C**). The adhesion force varied depending on substrate type due to differences in surface groups; steel surfaces exhibit adhesion through metal complexation, while adhesion to skin and glass primarily occurs through hydrogen bonds.

When utilized as an e-skin, excellent biocompatibility is essential for the ionogels.[1b] The in vitro cytocompatibility of the samples was assessed using NIH/3T3 mouse fibroblasts. As shown in **Figure 6D**, most cells in all samples remained viable,

appearing green, after 1 day and 3 days of cultivation. Furthermore, cell viability was quantitatively evaluated after 1 day and 3 days of cultivation, revealing that the cell viability of all samples exceeded 90% at both time points (**Figure 6E**). These results, combined with the live/dead assay, confirmed the excellent in vitro cytocompatibility of the samples, thereby supporting their potential application in biosensors and biomedicine.

2.4. Sensing Performance of the Strain-Temperature Dual Modal E-skin

Compared to recently reported iono/hydrogels that excel in only a single property, HDDNI integrated high adhesiveness and elasticity while maintaining strain-stiffening behavior, recyclability, and full self-healing capability. This unique combination of properties was clearly demonstrated in **Figure S14** and summarized in **Table S1**, where the radar chart provides a comprehensive, visual comparison of our material's performance across several key characteristics.[29] Unlike conventional iono/hydrogels, which typically exhibit trade-offs between these properties, our material achieves a well-balanced multifunctionality. This innovation is made possible by the hierarchical dynamic double-network structure, which effectively overcomes the performance compromises observed in previous designs. Meanwhile, due to the highly conductivity of DES, HDDNI showed high conductivity of 5 ms/cm (**Figure S15**). These qualities highlighted HDDNI's strong potential as a promising candidate for next-generation functional e-skins.

As a proof of concept, HDDNI could be utilized as a flexible conductor for fabrication of strain-temperature dual-modal e-skin with a multi-layered structure (as illustrated in **Figure 7A**).[17b] Notably, this e-skin exhibited high linearity in mechanoelectrical responsive performance over a wide strain range of up to 500%, with a high gauge factor (GF) of 1.6 (**Figure S16**). Meanwhile, thanks to the high elasticity of HDDNI, the e-skin's state-independent property ensured that relative resistance changes solely depend on external strain and remain unaffected by the deformation state.[17a] As shown in **Figure 7B**, the resistance-strain curve exhibited a nearly negligible hysteresis loop within the range of 0-200%, indicating that the resistance during stretching was equal to that during releasing. This contrasts with many reported hydrogel and/or ionogel-based sensors that display state-dependent characteristics, leading to poor sensing accuracy and limiting their application in human motion sensing. Meanwhile, this study evaluated the performance of an HDDNI-based e-skin at ultralow strain.

Figure 7C showed the e-skin's electronic patterns response to strains ranging from the original state to ±0.5% during the stepwise loading-unloading process, suggesting the e-skin can not only detect a 0.5% strain but also differentiate a 0.5% strain variation, indicating a high level of precision and sensitivity in strain detection. Additionally, the HDDNI-based e-skin exhibitd a rapid response time[30] of only 120 ms in both loading and unloading processes under the strain of 0.5%.

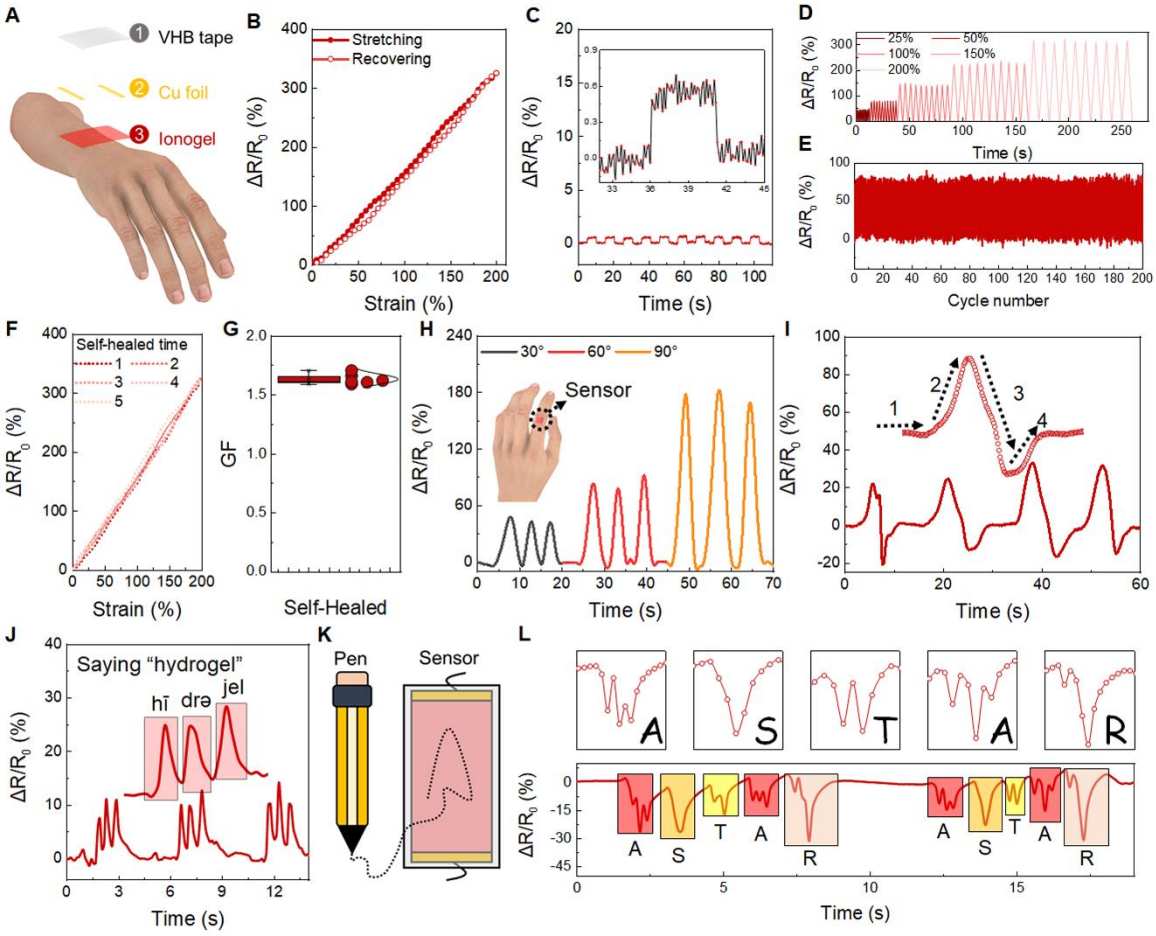

Figure 7. Mechanoelectronical responsiveness and practical application of the HDDNI-based e-skin. A) Schematic of the multi-layered structure of the HDDNI-based e-skin; **B)** Relative resistance ($\Delta R/R_0$) variations of HDDNI from 0–200%; **C)** Resistance patterns of HDDNI during stepwise loading-unloading tests at 0.5% deformation; **D)** Resistance variations of the e-skin under various maximum strains during cyclic testing (25, 50, 100, 150, and 200%); **E)** Resistance patterns of the e-skin under 200 stretching cycles at a maximum strain of 50%; **F)** Relative resistance ($\Delta R/R_0$) variations of the e-skins in different self-healing processes with 200% maximum strain; **G)** The summary of the GF of the ionogel during the cutting-healing process; **H)** Electronic patterns of the attached e-skin when the finger bends at different angles; **I)** Electronic patterns during wrist bending movements; **J)** Electromechanical response of the e-skin during speaking the English word of hydrogel; **K)** Schematic illustration for the configuration of flexible touch keyboard; **L)** Signature sensing waveforms during writing different english letters.

To our best knowledge, e-skin sensors should be able to detect a wide range of skin deformations. The good elasticity of HDDNI ensured outstanding cyclic stability of the corresponding e-skin in the cyclic test. Among a wide range of maximum strains (25, 50, 100, 150, and 200%), the sensor consistently exhibited remarkable cyclic stability, as shown in **Figure 7D**. Moreover, we performed 200 uninterrupted cyclic tests with a maximum strain of 50%. **Figure 7E** showed no significant shift in the baseline of the electronic patterns, indicating the sensor's good anti-fatigue capability. Furthermore, as shown in **Figure S17**, the corresponding response and recovery curves exhibit stable sensing performance. Utilizing its exceptional self-healing capability, as demonstrated in the above sections, the HDDNI-based e-skin maintained stable sensing performance through multiple cutting-healing cycles. The resistance-strain curves of the sensor at different cutting-healing cycles exhibited significant overlap with its original state (**Figure 7F**). Moreover, the GF of the e-skin remained stable across various healing intervals (first = 1.71, second = 1.59, third = 1.61, fourth = 1.61, fifth = 1.62) compared to the original sensor, indicating its excellent stability and reproducibility (**Figure 7G**). These findings underscored the durable and adaptable nature of the HDDNI-based e-skin, positioning it as a promising candidate for diverse, dynamic applications requiring high-performance standards.

Due to its versatile characteristics, the HDDNI-based e-skin could adapt to intricate deformations and a wide range of strains, making it promising for use in wearable electronic devices to recognize various human activities comprehensively. As the finger bending angles were at 30°, 60°, and 90°, the characteristic resistance variation was approximately ~40%, ~80%, and ~180%, respectively (**Figure 7H**). Additionally, the movement of the wrist bending could be divided into three clear stages: the initial state, backward motion, and forward motion. These above stages were clearly depicted in the electronic patterns, where the initial stage served as the reference signal platform, and two subsequent opposite peaks corresponded to subsequent steps (**Figure 7I**). These delicate physiological signals hold promise for applications in personal health monitoring and medical diagnostic systems.

The above advancements of the HDDNI-based e-skin have opened up new possibilities in information and communication devices. When applied to the human larynx, the HDDNI-based e-skin can aid in phonetic recognition. In **Figure 7J**, the three distinct signal peaks corresponded to the differentsyllables of "hydrogel", highlighting

its promise for integration into wearable devices for voice recognition and phonatory rehabilitation. **Figure 7K** illustrates the device configuration of a flexible touch keyboard. This touch keyboard could accurately respond to English letters such as “A”, “S”, “T”, “A”, and “R” with pressure amplitude, writing speed, and motion tracking influencing output signal intensity (**Figure 7L**). Various electronic signal peaks corresponding to different letters during writing indicate potential applications in personalized signature identification, anti-counterfeiting measures, and flexible displays.

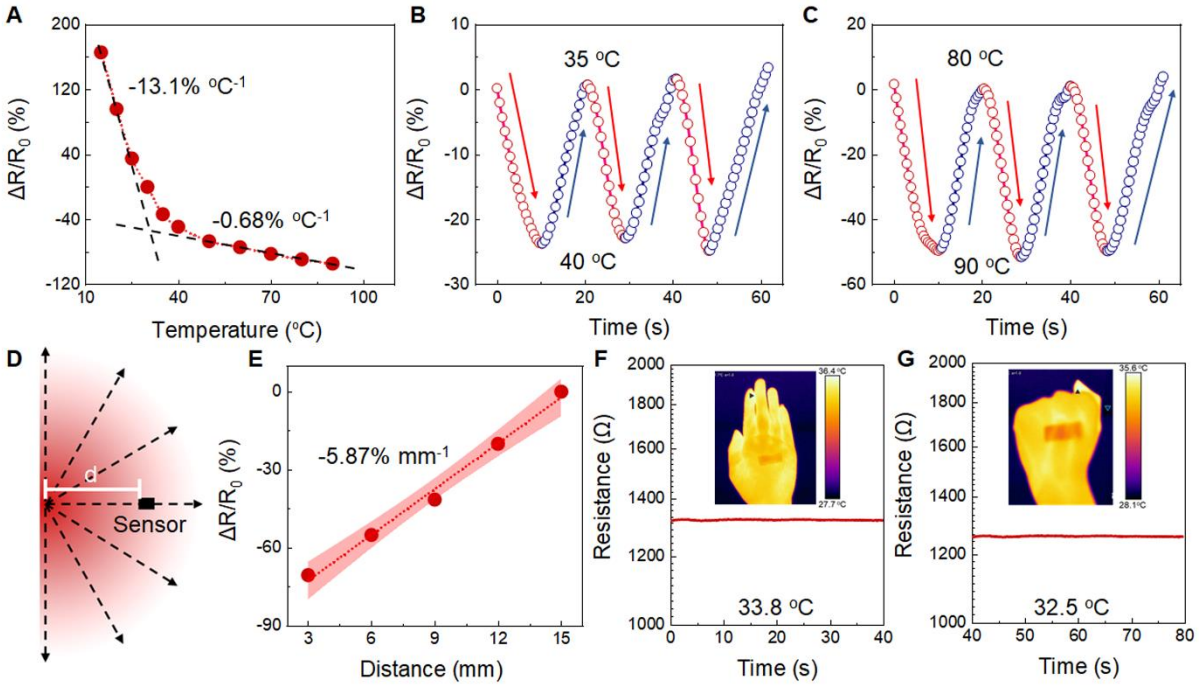

Figure 8. Thermalectronical responsiveness and practical application of the HDDNI-based flexible temperature e-skin. A) Resistance–temperature relative curve of the HDDNI-based e-skin in a wide temperature range (10–90 °C); The uninterrupted temperature sweeping electronic patterns at **B)** room temperature (35–40 °C) and **C)** extremely high temperature (80–90 °C); **D)** Schematic illustration of the distance-dependent thermal sensing mechanisim; **E)** Electronic patterns of the resistance-distance curve; Monitoring the temperature of **F)** palms and **G)** backs of the hand.

The ionogel’s high environmental stability and thermosensitive capability enabled the development of a thermal sensor. A temperature coefficient of resistance (TCR) was used to evaluate the sensitivity of the thermal response and was defined as TCR = $[(R_T - R_0)/R_0)]/\delta T$, where R_T is the instantaneous resistance at the measured temperature, and R_0 is the original resistance. Due to the temperature-dependent migration rates of ions, this sensor exhibited a negative thermo-sensitive characteristic

with two TCR values (-13.1 and 0.68 $°C^{-1}$) (**Figure 8A**). Notably, the low saturated vapor pressure and high thermal stability of the DES allowed for an extensive temperature range of application (10–90 °C), significantly wider than that of most reported thermosensitive sensors.[31] Additionally, the repeatability and reproducibility of the thermosensitive capability were crucial for practical sensor applications. Specifically, cyclic thermal simulations were conducted between near-body surface temperatures (35–40 °C) and high temperatures (80–90 °C). As shown in **Figure 8B** and **C**, the sensor exhibited a nearly constant response during the cyclic test, indicating excellent durability.

The varying heat energy along the temperature field notably affected the electrical signal, emphasizing the obvious influence of the distance between the object and the heat source. As shown in **Figure 8D**, the temperature sensor's resistance varied with the spacing distance. A longer distance resulted in a higher resistance, with the thermosensitive response to the spacing distance being approximately -5.87 °C mm^{-1} (**Figure 8E**). Furthermore, we integrated the sensor into an indicator for quantitative human temperature measurement, focusing on real-time monitoring of the palms and backs of the hand. Simultaneously, an infrared thermography camera was used for instant temperature detection. The e-skin attached to the palm showed a resistance value of approximately 1323 Ω, corresponding to the body's normal temperature (33.8 °C), while the response current sharply decreased to about 1257 Ω when the e-skin was attached to the back of the hand (**Figure 8F and 8G**). These findings were consistent with the infrared thermal imaging temperature, confirming the accuracy of the temperature e-skin.

3. Conclusion

In summary, by integrating dynamic covalent and non-covalent bonds, we have developed a multifunctional, recyclable e-skin, mimicking the complex properties of human skin, such as, strain-stiffening, self-healability, and elasticity. The hierarchical dynamic network within ionogels ensures recyclability and self-healing capability without compromising mechanical properties, while maintaining strain-stiffening behavior. The dynamic covalent bonds enhance cohesive energy, ensuring high elasticity with minimal energy loss during cyclic deformation. Additionally, strong adhesive properties, driven by hydrogen bonding and electrostatic interactions, ensure reliable sensor performance. As a proof of concept, the strain-temperature dual-modal

e-skin demonstrates recyclability, high sensitivity, reliability, and state-independent characteristics, making it a promising candidate for next-generation sustainable wearable electronics.

4. Experimental Sections

Materials. Choline chloride (ChCl, 99%), and glycerol (99.8%), acrylamide (AAm, 99%), N,N'-methylenebisacrylamide (MBAA, 98%), N,N'-bis(acryloyl)cystamine (BAC, 98%), [(2-(methacryloyloxy) ethyl] dimethyl-(3-sulfopropyl) ammonium hydroxide (SBMA, ≥97%), 2,2-diethoxyacetophenone (DEAP, 95%), were all purchased from Sigma-Aldrich. The VHB tapes were purchased from Minnesota Mining and Manufacturing (3M) Co. Notably, the ChCl–glycerol DES was prepared by mixing the ChCl and glycerol with a 1:2 molar ratio at 70 °C under stirring for 10 min, following the reported work.[32] NIH/3T3 mouse fibroblasts cells were purchased from the American Type Culture Collection. Dulbecco's modified Eagle's medium (DMEM), fetal bovine serum and 1% penicillin-streptomycin from Gibco were purchased from Fisher Scientific. Alamarblue, NucBlue Live ReadyProbes, fluorescein diacetate and propidium iodide were bought from Life Technologies.

Preparation of the hierarchical dynamic double-network ionogel (HDDNI). AAm (0.7 g), SBMA (0.3 g), DEAP (10 uL), and varying amounts of BAC (3, 6, and 9 mg) were dissolved in 2 mL ChCl-glycerol DES under stirring in a nitrogen atmosphere until completely dissolved, forming a homogeneous solution. The solution was then transferred into a poly(tetrafluoroethylene) (PTFE) mold with a designed shape and cured under a UV light (λ = 365 nm, power: 8 W) for 1 hour. For comparison, a hierarchical non-dynamic double-network ionogel (HNDNI) was synthesized using N,N'-methylenebisacrylamide (MBAA) as the cross-linker, with conditions identical to those for HDDNI-2. A dynamic single-network ionogel (DSNI) was also prepared without any cross-linker, under the same conditions as HDDNI-2. Additionally, a P(AAm-co-SBMA) hydrogel was synthesized using water as the solvent instead of DES, without any cross-linker, while maintaining the other conditions as in HDDNI-2.

Supporting Information

Supporting Information is available from the Wiley Online Library or from the author.

Acknowledgements

This project is supported by the Agency for Science, Technology and Research (A*STAR) under its RIE2025 Manufacturing, Trade and Connectivity (MTC) Programmatic Funding (Grant No. M22K9b0049) and MedTech Thematic Grant (Grant No. M24N9b0126). X.Y. acknowledges support from the China Scholarship Council Scholarship (Grant No. 202306630076).

References

[1] a) M. Wang, Y. Luo, T. Wang, C. Wan, L. Pan, S. Pan, K. He, A. Neo, X. Chen, Advanced Materials **2021**, 33, 2003014; b) W. Zhang, B. Wu, S. Sun, P. Wu, Nature Communications **2021**, 12, 4082.

[2] a) J. Chen, Q. Peng, X. Peng, L. Han, X. Wang, J. Wang, H. Zeng, ACS Applied Polymer Materials **2020**, 2, 1092; b) M. Vatankhah-Varnosfaderani, A. N. Keith, Y. Cong, H. Liang, M. Rosenthal, M. Sztucki, C. Clair, S. Magonov, D. A. Ivanov, A. V. Dobrynin, S. S. Sheiko, Science **2018**, 359, 1509.

[3] a) N. T. P. Vo, T. U. Nam, M. W. Jeong, J. S. Kim, K. H. Jung, Y. Lee, G. Ma, X. Gu, J. B. H. Tok, T. I. Lee, Z. Bao, J. Y. Oh, Nature Communications **2024**, 15, 3433; b) A. Rafsanjani, F. B. Coulter, A. R. Studart, Matter **2022**, 5, 1990.

[4] a) M. Kang, R. Qu, X. Sun, Y. Yan, Z. Ma, H. Wang, K. Yan, W. Zhang, Y. Deng, Advanced Materials **2023**, 35, 2309629; b) S. Shi, Y. Ming, H. Wu, C. Zhi, L. Yang, S. Meng, Y. Si, D. Wang, B. Fei, J. Hu, Advanced Materials **2024**, 36, 2306435.

[5] a) W. Wang, Y. Jiang, D. Zhong, Z. Zhang, S. Choudhury, J.-C. Lai, H. Gong, S. Niu, X. Yan, Y. Zheng, C.-C. Shih, R. Ning, Q. Lin, D. Li, Y.-H. Kim, J. Kim, Y.-X. Wang, C. Zhao, C. Xu, X. Ji, Y. Nishio, H. Lyu, J. B. H. Tok, Z. Bao, Science **2023**, 380, 735; b) X. Yang, W. Chen, Q. Fan, J. Chen, Y. Chen, F. Lai, H. Liu, Advanced Materials **2024**, 36, 2402542; c) J. B. Fudge, Nature Biotechnology **2023**, 41, 766; d) Q. Huang, Y. Jiang, Z. Duan, Z. Yuan, Y. Wu, J. Peng, Y. Xu, H. Li, H. He, H. Tai, IEEE Sensors Journal **2023**, 23, 13789; e) Z. Yuan, H. Li, Z. Duan, Q. Huang, M. Zhang, H. Zhang, J. Guo, Y. Jiang, H. Tai, Sensors and Actuators A: Physical **2024**, 369, 115202; f) Q. Huang, Y. Jiang, Z. Duan, Y. Wu, Z. Yuan, M. Zhang, Q. Zhao, Y. Zhang, B. Liu, H. Tai, Nano Energy **2023**, 118, 108997; g) Q. Huang, Y. Jiang, Z. Duan, Y. Wu, Z. Yuan, J. Guo, M. Zhang, H. Tai, Nano Energy **2024**, 126, 109689.

[6] a) Y. Wang, X. Yu, Q. Hou, X. Fan, Journal of Materials Chemistry C **2024**, 12, 7351; b) C.-C. Yan, W. Li, Z. Liu, S. Zheng, Y. Hu, Y. Zhou, J. Guo, X. Ou, Q. Li, J. Yu, L. Li, M. Yang, Q. Liu, F. Yan, Advanced Functional Materials **2024**, 34, 2314408; c) X. Fan, S. Liu, Z. Jia, J. J. Koh, J. C. C. Yeo, C.-G. Wang, N. E. Surat'man, X. J. Loh, J. Le Bideau, C. He, Z. Li, T.-P. Loh, Chemical Society Reviews **2023**, 52, 2497; d) X. Fan, Y. Luo, K. Li, Y. J. Wong, C. Wang, J. C. C. Yeo, G. Yang, J. Li, X. J. Loh, Z. Li, X. Chen, Advanced Materials **2024**, 36, 2407398.

[7] a) Y. Mao, L. Wang, Z. Wu, D. Ji, H. Sheng, X. Chang, Y. Zhu, Composites Communications **2023**, 44, 101769; b) T. Ye, X. Zhang, J. Wen, X. Sun, D. He, W. Li, Chemical Engineering Journal **2023**, 477, 147182.

[8] W. Li, L. Li, S. Zheng, Z. Liu, X. Zou, Z. Sun, J. Guo, F. Yan, Advanced Materials **2022**, 34, 2203049.

[9] a) Y. Ye, H. Oguzlu, J. Zhu, P. Zhu, P. Yang, Y. Zhu, Z. Wan, O. J. Rojas, F. Jiang, Advanced Functional Materials **2023**, 33, 2209787; b) S. Chen, L. Sun, X. Zhou,

Y. Guo, J. Song, S. Qian, Z. Liu, Q. Guan, E. Meade Jeffries, W. Liu, Y. Wang, C. He, Z. You, Nature Communications **2020**, 11, 1107; c) I. Jeon, J. Cui, W. R. K. Illeperuma, J. Aizenberg, J. J. Vlassak, Advanced Materials **2016**, 28, 4678.
[10] J. Xu, Y. Jiang, L. Gao, Journal of Materials Chemistry B **2023**, 11, 221.
[11] X. Fan, J. Zheng, J. C. C. Yeo, S. Wang, K. Li, J. K. Muiruri, N. Hadjichristidis, Z. Li, Angewandte Chemie International Edition **2024**, n/a, e202408969.
[12] X. Yu, Y. Zheng, H. Zhang, Y. Wang, X. Fan, T. Liu, Chemistry of Materials **2021**, 33, 6146.
[13] a) M. Liao, P. Wan, J. Wen, M. Gong, X. Wu, Y. Wang, R. Shi, L. Zhang, Advanced Functional Materials **2017**, 27, 1703852; b) S. Wang, Y. Fang, H. He, L. Zhang, C. a. Li, J. Ouyang, Advanced Functional Materials **2021**, 31, 2007495.
[14] B. B. Hansen, S. Spittle, B. Chen, D. Poe, Y. Zhang, J. M. Klein, A. Horton, L. Adhikari, T. Zelovich, B. W. Doherty, B. Gurkan, E. J. Maginn, A. Ragauskas, M. Dadmun, T. A. Zawodzinski, G. A. Baker, M. E. Tuckerman, R. F. Savinell, J. R. Sangoro, Chemical Reviews **2021**, 121, 1232.
[15] P. Yao, Q. Bao, Y. Yao, M. Xiao, Z. Xu, J. Yang, W. Liu, Advanced Materials **2023**, 35, 2300114.
[16] G. Zhang, S. Chen, Z. Peng, W. Shi, Z. Liu, H. Shi, K. Luo, G. Wei, H. Mo, B. Li, L. Liu, ACS Applied Materials & Interfaces **2021**, 13, 12531.
[17] a) X. Yu, H. Zhang, Y. Wang, X. Fan, Z. Li, X. Zhang, T. Liu, Advanced Functional Materials **2022**, 32, 2204366; b) X. Yu, Y. Wang, H. Zhang, Z. Li, Y. Zheng, X. Fan, Y. Lv, X. Zhang, T. Liu, Chemistry of Materials **2023**, 35, 9287.
[18] H. Hiratani, C. Alvarez-Lorenzo, J. Chuang, O. Guney, A. Y. Grosberg, T. Tanaka, Langmuir **2001**, 17, 4431.
[19] Y. Ma, Q. Dong, ACS Sustainable Chemistry & Engineering **2023**, 11, 12843.
[20] X. Jin, H. Jiang, F. Qiao, W. Huang, X. Bao, Z. Wang, Q. Hu, Journal of Applied Polymer Science **2021**, 138, 49697.
[21] C. Wang, K. Deitrick, J. Seo, Z. Cheng, N. S. Zacharia, R. A. Weiss, B. D. Vogt, Macromolecules **2019**, 52, 6055.
[22] a) X. Yu, Y. Zheng, Y. Wang, H. Zhang, H. Song, Z. Li, X. Fan, T. Liu, Chemistry of Materials **2022**, 34, 1110; b) R. G. Ricarte, S. Shanbhag, D. Ezzeddine, D. Barzycki, K. Fay, Macromolecules **2023**, 56, 6806.
[23] a) G. Zhang, X. Cai, C. Li, J. Yao, W. Liu, C. Qiao, G. Li, Q. Wang, J. Han, ACS Applied Polymer Materials **2023**, 5, 3622; b) Y. Wang, Y. Liu, R. Plamthottam, M. Tebyetekerwa, J. Xu, J. Zhu, C. Zhang, T. Liu, Macromolecules **2021**, 54, 3832.
[24] a) J. Canadell, H. Goossens, B. Klumperman, Macromolecules **2011**, 44, 2536; b) Q. Zhang, D.-H. Qu, B. L. Feringa, H. Tian, Journal of the American Chemical Society **2022**, 144, 2022.
[25] R. Yang, Y. Yao, Z. Duan, Z. Yuan, H. Tai, Y. Jiang, Y. Zheng, D. Wang, Langmuir **2020**, 36, 3029.
[26] X. Wang, Y.-l. Wang, X. Yang, Z. Lu, Y. Men, J. Sun, Macromolecules **2021**, 54, 10767.
[27] J. Deng, X. Kuang, R. Liu, W. Ding, A. C. Wang, Y.-C. Lai, K. Dong, Z. Wen, Y. Wang, L. Wang, H. J. Qi, T. Zhang, Z. L. Wang, Advanced Materials **2018**, 30, 1705918.
[28] B. Guo, M. Yao, S. Chen, Q. Yu, L. Liang, C. Yu, M. Liu, H. Hao, H. Zhang, F. Yao, J. Li, Advanced Functional Materials **2024**, n/a, 2315656.
[29] a) S. Yuan, J. Bai, S. Li, N. Ma, S. Deng, H. Zhu, T. Li, T. Zhang, Advanced Functional Materials **2024**, 34, 2309626; b) Y. Long, B. Jiang, T. Huang, Y. Liu, J. Niu, Z. L. Wang, W. Hu, Advanced Functional Materials **2023**, 33, 2304625; c) S. Wei, J. Xu, W. Zhao, X. Li, W. Zhao, S. Yan, Advanced Functional Materials **2024**, n/a,

2408648; d) X. Dai, Y. Wu, Q. Liang, J. Yang, L.-B. Huang, J. Kong, J. Hao, Advanced Functional Materials **2023**, 33, 2304415; e) A. Roy, S. Zenker, S. Jain, R. Afshari, Y. Oz, Y. Zheng, N. Annabi, Advanced Materials **2024**, 36, 2404225; f) J. Zhang, Z. Ma, M. Li, M. Lou, H. Wang, L. Jia, Advanced Functional Materials **2024**, n/a, 2415694; g) L. Yu, C. Huang, Y. Gong, S. Zheng, P. Zhou, X. Zhang, Z. Zou, X. Lyu, Macromolecules **2024**, 57, 2339; h) Y. Sun, Y. Cheng, L. Shi, J. Sun, S. Chen, R. Wang, Advanced Functional Materials **2024**, 34, 2401808.

[30] Z. Duan, Y. Jiang, S. Wang, Z. Yuan, Q. Zhao, G. Xie, X. Du, H. Tai, ACS Sustainable Chemistry & Engineering **2019**, 7, 17474.

[31] a) B. W. An, S. Heo, S. Ji, F. Bien, J.-U. Park, Nature Communications **2018**, 9, 2458; b) J. Bang, W. S. Lee, B. Park, H. Joh, H. K. Woo, S. Jeon, J. Ahn, C. Jeong, T.-i. Kim, S. J. Oh, Advanced Functional Materials **2019**, 29, 1903047; c) W. Honda, S. Harada, S. Ishida, T. Arie, S. Akita, K. Takei, Advanced Materials **2015**, 27, 4674; d) Q. Hua, J. Sun, H. Liu, R. Bao, R. Yu, J. Zhai, C. Pan, Z. L. Wang, Nature Communications **2018**, 9, 244; e) T. Q. Trung, S. Ramasundaram, B.-U. Hwang, N.-E. Lee, Advanced Materials **2016**, 28, 502; f) W. He, G. Li, S. Zhang, Y. Wei, J. Wang, Q. Li, X. Zhang, ACS Nano **2015**, 9, 4244.

[32] G. Ge, K. Mandal, R. Haghniaz, M. Li, X. Xiao, L. Carlson, V. Jucaud, M. R. Dokmeci, G. W. Ho, A. Khademhosseini, Advanced Functional Materials **2023**, 33, 2207388.